Journal of Computational Physics 229 (2010) 3155–3170

Contents lists available at ScienceDirect

Journal of Computational Physics

journal homepage: www.elsevier.com/locate/jcp

High order matched interface and boundary methods for the Helmholtz equation in media with arbitrarily curved interfaces

Shan Zhao *

Department of Mathematics, University of Alabama, Tuscaloosa, AL 35487, USA

ARTICLE INFO

Article history:
Received 21 May 2009
Received in revised form 21 December 2009
Accepted 23 December 2009
Available online 4 January 2010

Keywords:
High order finite difference methods
Inhomogeneous media
Arbitrarily curved interface
Staircasing error
Step-index waveguide
Matched interface and boundary method

ABSTRACT

This work overcomes the difficulty of the previous matched interface and boundary (MIB) method in dealing with interfaces with non-constant curvatures for optical waveguide analysis. This difficulty is essentially bypassed by avoiding the use of local cylindrical coordinates in the improved MIB method. Instead, novel jump conditions are derived along global Cartesian directions for the transverse magnetic field components. Effective interface treatments are proposed to rigorously impose jump conditions across arbitrarily curved interfaces based on a simple Cartesian grid. Even though each field component satisfies the scalar Helmholtz equation, the enforcement of jump conditions couples two transverse magnetic field components, so that the resulting MIB method is a full-vectorial approach for the modal analysis of optical waveguides. The numerical performance of the proposed MIB method is investigated by considering interface problems with both constant and general curvatures. The MIB method is shown to be able to deliver a fourth order of accuracy in all cases, even when a high frequency solution is involved.

1. Introduction

This work overcomes the difficulty of dealing with non-constant curvatures in the recently developed high order matched interface and boundary (MIB) method [39] for eigenmode analysis of optical waveguides with dielectric interfaces. As basic building blocks of optoelectronic devices, step-index optical waveguides are often of regular cross-sections, such as rectangle and circle. However, in recent years, there has been an increased interest in the design of waveguides with arbitrary refractive profiles to address modern application needs [6]. For the purpose of test and design of such devices, advanced numerical approaches are called for.

Consider a linear isotropic optical waveguide which is homogeneous along the z-direction. Its cross-section typically consists of two regions: an inner region Ω^-, or core, and an infinite outer region Ω^+, or cladding. See Fig. 1(a). Across the interface Γ separating Ω^- and Ω^+, the permittivity ϵ is discontinuous, while the permeability $\mu = 1$ throughout. In this paper, we will assume the dielectric interface Γ being arbitrarily curved and C^1 continuous. Except on Γ, a Cartesian component u of the magnetic field intensity **H** or electric field intensity **E** satisfies the scalar Helmholtz equation

$$\frac{\partial^2 u}{\partial x^2} + \frac{\partial^2 u}{\partial y^2} + \omega^2 \epsilon u = \beta^2 u, \quad \text{in} \quad \Omega^- \cup \Omega^+, \tag{1}$$

where β is the propagation constant and $\omega = 2\pi/\lambda$ is the free space wavenumber with λ being the free space wavelength. Across Γ, field solutions in both media are related analytically via the jump conditions

* Tel.: +1 205 3485155; fax: +1 205 3487067.
E-mail address: szhao@bama.ua.edu

0021-9991/$ - see front matter © 2009 Elsevier Inc. All rights reserved.
doi:10.1016/j.jcp.2009.12.034

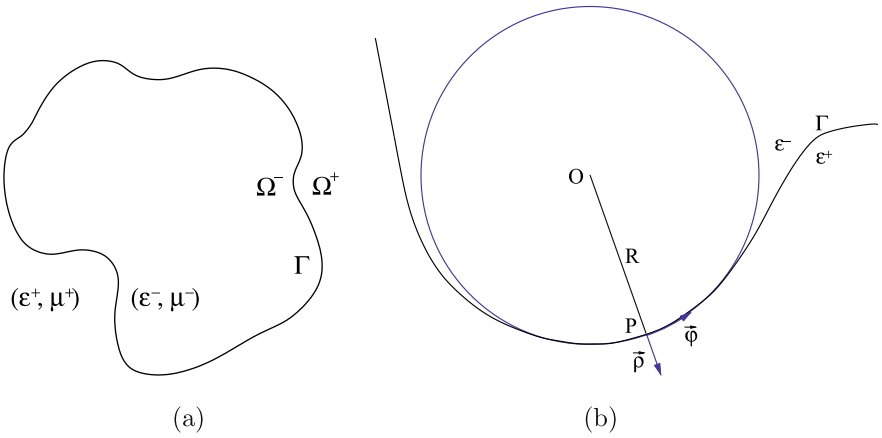

Fig. 1. (a) A typical cross-section of a optical waveguide with arbitrarily curved interface. (b) The osculating circle at an interface point P and the corresponding local coordinate.

$$\hat{\mathbf{n}} \times (\mathbf{E}^+ - \mathbf{E}^-) = \mathbf{0}, \quad \hat{\mathbf{n}} \cdot (\epsilon^+ \mathbf{E}^+ - \epsilon^- \mathbf{E}^-) = \mathbf{0}, \quad \hat{\mathbf{n}} \times (\mathbf{H}^+ - \mathbf{H}^-) = \mathbf{0}, \quad \hat{\mathbf{n}} \cdot (\mu^+ \mathbf{H}^+ - \mu^- \mathbf{H}^-) = \mathbf{0}, \tag{2}$$

where the superscript, − or +, denotes the limiting value of a function from one side or the other of the interface. Here $\hat{\mathbf{n}}$ is the unit vector normal to the interface, pointing from Ω^- into Ω^+.

In the past two decades, numerous numerical methods have been proposed to solve optical waveguides, including finite difference method [26], finite element method [19], pseudospectral method [3], discontinuous Galerkin method [8], and so on. The general trend in the field has been to move from the scalar methods which solve a single field component to the the full-vectorial methods that solve more than one field components simultaneously. The first major progress was due to Stern [27] who proposed a semivectorial finite difference method, which essentially incorporates an averaging of the permittivity into the scalar formulation. Stern's scheme has been further improved by Vassallo [31] to yield uniformly second order convergence for step-index waveguides. Since then, many full-vectorial methods have been presented, see for example [1,34,24,13,33]. The evolution from scalar methods to full-vectorial approaches was primarily driven by the need of improving numerical accuracy. In fact, a simple mathematical justification of such a development is that interface jump conditions (2) couple more than one field components, even though each component satisfies the scalar Helmholtz Eq. (1). Thus, a full-vectorial approach in which jump conditions (2) are accounted for in some manner, will be more accurate than a scalar method. For the same reason, in order to formulate a optical solver whose order of accuracy is higher than two, a higher order interface scheme that appropriately enforces jump conditions in the numerical discretization, is essential [40].

Many interface schemes for optical waveguides have been developed to enforce jump conditions (2) on straight dielectric interfaces [32,28,12,5,35,29]. Typically, to achieve higher order convergence, higher order jump conditions furthered derived from (2) and Maxwell's equations are matched via the Taylor series expansions in these schemes. By properly incorporating jump conditions into infinite series solution of the two-dimensional (2D) Helmholtz equation involving Bessel functions, sines and cosines, several full-vectorial finite difference equation methods have been constructed by Hadley [14–17]. Up to 6th order accuracy has been attained for 2D straight interface problems [16]. However, the extension of these interface schemes to ultra high order could be technically challenging, because formidable algebra is involved in deriving ultra high order jump conditions. Such a difficulty has been overcome in a recently developed matched interface and boundary (MIB) method, through introducing the concept of the iterative use of low order jump conditions [38]. Orders up to 12 have been numerically achieved in solving rectangular waveguide with a single straight interface [38].

In order to secure high accuracy in solving optical waveguides with curved interfaces, besides the rigorous enforcement of jump conditions (2), sophisticated numerical treatments to accommodate the complicated geometry associated with arbitrarily curved interfaces are indispensable. In resolving arbitrarily curved boundary, one popular way in the literature is fitting the grid to the boundary. For some numerical methods, such as boundary element method [23] and method of line analysis [36], the grid fitting can be simply attained via sampling exactly on the interfaces. Thus, the staircasing error is not an issue when applying these methods to photonic simulations [23,36]. For other methods, body-fitted grids can be generated through the use of unstructured grids or body-conforming mesh transformations. For example, a non-uniform triangular mesh has been adopted in a full-vectorial finite difference method [18]. For the finite element methods, curvilinear/isoparametric elements [20,7] have been employed to modify the triangular mesh near the interfaces. Similarly, circular and/or elliptical arcs instead of straight arc are utilized in a boundary integral method for representing arbitrarily shaped waveguides [6]. A curvilinear mapping technique has been introduced in a multidomain pseudospectral method [3] to cope with general curved interfaces, and spectral convergence has been reported for curved interfaces with constant curvature [3].

In the present paper, we are more interested in constructing Cartesian grid methods for optical simulation with curved dielectric interfaces. Comparing with body-fitted grid methods, Cartesian grid methods are relatively simple and avoid the

complicated procedure of mesh generation. Moreover, Cartesian grid methods could lend themselves to many contemporary software packages which are mainly developed for Cartesian grids. For solving interface problems associated with Poisson equations, Cartesian grid methods have been shown to be able to represent arbitrary interfaces [21,9,30] and deliver higher order of accuracy [42]. For optical waveguides with curved interfaces, the first Cartesian grid method was suggested by Chiang et al. in [4]. The jump conditions (2) are rigorously imposed in terms of local cylindrical components of **E** and **H** in [4] so that the second order convergence has been achieved. Recently, we have proposed a novel full-vectorial matched interface and boundary (MIB) method [39], which also implements jump conditions based on local cylindrical components. Via iteratively matching jump conditions, the fourth order convergence has been numerically confirmed for optical fibers with constant curvature [39].

However, the previous MIB approach [39] is cumbersome to be generalized to accommodate arbitrarily curved interfaces with non-constant curvatures. A complicated process has to be taken, which involves the generation of a lot of osculating circles surrounding the interface. Within each osculating circle, forward and backward coordinate transformations shall be performed so that jump conditions (2) can be satisfied in the local cylindrical coordinate, while eigenmodes are still sought in terms of global Cartesian components. Besides the tedious implementation, there are also new mathematical issues needed to be taken care of. For example, in order to treat negative curvature, the MIB scheme needs to be reformulated to account for the cases where the centers of osculating circles are switched to the other hand side of the interface. Moreover, when the curvature variants rapidly or when a coarse grid is used, there is a mismatching between the osculating arcs and the interface. The impact of such a mismatching on the accuracy of the MIB scheme [39] is unclear.

The objective of this paper is to overcome the aforementioned difficulty of the MIB method, by introducing a simpler procedure to enforce jump conditions. The proposed MIB method can then attain the fourth order of accuracy for optical simulation with arbitrarily curved interfaces. The full-vectorial MIB method developed in this work and in the previous studies [38,39] are all reformulated from a scalar MIB method, originally proposed in [40] for solving Maxwell's equations with straight interfaces. The scalar MIB method has been generalized to treat curved interfaces for solving the Poisson equation [42]. Recently, the application of the MIB method as a fictitious domain boundary closure scheme for high order finite differences has been considered in [37,41].

In the proposed MIB method and the previous MIB schemes [40,42,38,39,37,41], the use of fictitious nodes is an important step in enforcing the jump/boundary conditions. In terms of using fictitious points or ghost cells, the MIB shares some similarities with the ghost fluid method (GFM), originally developed by Fedkiw et al. [9] for treating contact discontinuities in the inviscid Euler equations. The GFM has been subsequently generalized as a sharp interface scheme for solving Poisson equation with jump conditions [22], and as a second order accurate symmetric scheme [10,25] and a fourth order accurate non-symmetric scheme [11], respectively, for solving Poisson equation with Dirichlet boundary conditions on irregular domains. In both MIB and GFM, the solution is smoothly extended by some means across the interface or boundary into a ghost fluid. On irregular grid points, when the finite difference stencil refers to a node from the other side of the interface or outside the boundary, a ghost fluid value instead of the real one will be supplied. The major difference between the GFM and MIB is on how to impose jump conditions for the smooth extension. In the GFM, the jump in the normal derivative is correctly captured through a projection to Cartesian coordinate directions, while the jump in the tangential derivatives is neglected [22]. This treatment contributes to the simplicity, robustness, and symmetry of the GFM, albeit limits the order of the GFM for the interface problems [22]. On the other hand, the jump conditions are always rigorously satisfied in the MIB method, so that the MIB typically achieves the fourth order of accuracy in solving curved interface problems [42,39].

The rest of this paper is organized as follows. Section 2 is devoted to theory and algorithm of the proposed full-vectorial MIB method. For completeness, the MIB method developed in [39] will be briefly described. Numerical tests are carried out to validate the proposed method in resolving interfaces with non-constant curvatures in Section 3. Finally, a conclusion ends this paper.

2. Theory and algorithm

In this section, a brief introduction to the mathematical background and setting of eigenmode analysis of optical waveguides is first given. The general procedure of the full-vectorial matched interface and boundary (MIB) methods will then be described. Interface treatment used in the previously developed MIB method [39] will be briefly reviewed. The difficulty associated with such a MIB method for dielectric interfaces with non-constant curvatures will be discussed. A new full-vectorial MIB method will then be proposed to circumvent this difficulty. Finally, the discretization details of the MIB schemes are presented.

2.1. Physical equations and boundary conditions

Consider a linear isotropic optical waveguide with a general material interface. A typical configuration is shown in Fig. 1(a). In this paper, we will assume the dielectric interface Γ being arbitrarily curved and C^1 continuous. Mathematically, the time-harmonic electromagnetic wave guiding is governed by the source-free Maxwell's equations. For simplicity, we will consider only equations for the magnetic field intensity **H**. Equations for the electric field intensity **E** can be similarly treated. Using Maxwell's equations, the following vector wave equation can be derived for **H**

$$\nabla \times \left(\frac{1}{\epsilon}\nabla \times \mathbf{H}\right) - \omega^2 \mu \mathbf{H} = 0, \quad \text{in } \Omega, \tag{3}$$

where ϵ and μ are, respectively, the relative permittivity and permeability coefficients, and $\omega = 2\pi/\lambda$ is the free space wavenumber with λ being the free space wavelength. Using vector analysis, Eq. (3) can be rewritten into the vector Helmholtz equations

$$\nabla^2 \mathbf{H} + \omega^2 \epsilon \mu \mathbf{H} = -\epsilon\left(\nabla \frac{1}{\epsilon} \cdot \nabla\right)\mathbf{H}, \quad \text{in} \quad \Omega. \tag{4}$$

Because the optical waveguides are normally homogeneous in the z-direction, one can assume the field $\mathbf{H}$ varies as $e^{-j\beta z}$ along the z-coordinate, where β is the propagation constant and $j = \sqrt{-1}$. Consequently, we have $\frac{\partial^2 \mathbf{H}}{\partial z^2} = -\beta^2 \mathbf{H}$ and $\frac{\partial(1/\epsilon)}{\partial z} = 0$, so that by eliminating the term $e^{-j\beta z}$, Eq. (4) reduces to

$$\nabla_t^2 \mathbf{H} + \omega^2 \epsilon \mu \mathbf{H} = \beta^2 \mathbf{H} - \epsilon\left(\nabla_t \frac{1}{\epsilon} \cdot \nabla_t\right)\mathbf{H}, \quad \text{in} \quad \Omega, \tag{5}$$

where ∇_t is the transverse part of ∇. Within each homogeneous medium, either Ω^- or Ω^+, the dielectric coefficient ϵ is a constant so that the singular term on the right hand side of (5) can be dropped

$$\nabla_t^2 \mathbf{H} + \omega^2 \epsilon \mu \mathbf{H} = \beta^2 \mathbf{H}, \quad \text{in} \quad \Omega^- \cup \Omega^+. \tag{6}$$

Thus, the Cartesian components of $\mathbf{H}$, denoting as (H^x, H^y, H^z), satisfy the scalar Helmholtz equation given in (1).

To recover the effect of the singular term being dropped in (5), the jump conditions (2) should be imposed on Γ in the numerical discretization. This is the essential theme underlying any interface scheme. In the following, we will consider the jump conditions (2) in terms of a local cylindrical coordinate. Let the curvature of Γ at an interface point P be κ. Then a segment of Γ surround P can be approximated via the osculating circle defined at P with the effective radius $R = 1/\kappa$. This gives rise to a local cylindrical coordinate system $(\vec{\rho}, \vec{\varphi}, \vec{z})$, see Fig. 1(b). On such a local grid system, Eq. (2) reduces to the following six zeroth order jump conditions for the cylindrical components of $\mathbf{E}$ and $\mathbf{H}$

$$[H^z] = 0, \quad [H^\varphi] = 0, \quad [H^\rho] = 0, \quad [E^z] = 0, \quad [E^\varphi] = 0, \quad [\epsilon E^\rho] = 0, \tag{7}$$

where $[u]$ denotes a function jump for a scalar function u, i.e., $[u] := \lim_{\rho \to R^+} u - \lim_{\rho \to R^-} u$.

In the following, we will derive necessary first order jump conditions for H^ρ and H^φ. Since the dielectric medium remains homogeneous along either the φ or z direction, some first order jump conditions can be directly derived by taking derivatives along these two directions

$$\left[\frac{\partial H^\varphi}{\partial \varphi}\right] = 0, \quad \left[\frac{\partial H^\rho}{\partial \varphi}\right] = 0, \quad \left[\frac{\partial H^z}{\partial z}\right] = 0, \tag{8}$$

Other necessary first order jump conditions can be derived by using Maxwell's equations. Consider the Gauss's law for magnetic field with $\mu = 1$

$$\nabla \cdot \mathbf{H} = \frac{1}{\rho}\frac{\partial}{\partial \rho}(\rho H^\rho) + \frac{1}{\rho}\frac{\partial H^\varphi}{\partial \varphi} + \frac{\partial H^z}{\partial z} = \frac{\partial H^\rho}{\partial \rho} + \frac{1}{\rho}H^\rho + \frac{1}{\rho}\frac{\partial H^\varphi}{\partial \varphi} + \frac{\partial H^z}{\partial z} = 0. \tag{9}$$

Since Eq. (9) is valid in both Ω^- and Ω^+, one can take jump values on both hand sides of Eq. (9)

$$\left[\frac{\partial H^\rho}{\partial \rho}\right] + \frac{1}{R}[H^\rho] + \frac{1}{R}\left[\frac{\partial H^\varphi}{\partial \varphi}\right] + \left[\frac{\partial H^z}{\partial z}\right] = 0. \tag{10}$$

With the last three jump values vanishing in Eq. (10), we thus have $\left[\frac{\partial H^\rho}{\partial \rho}\right] = 0$. To derive the last first order jump condition, we consider the time harmonic Maxwell equation for E^z

$$j\omega E^z = \frac{1}{\epsilon\rho}\left(\frac{\partial(\rho H^\varphi)}{\partial \rho} - \frac{\partial H^\rho}{\partial \varphi}\right) = \frac{1}{\epsilon}\frac{\partial H^\varphi}{\partial \rho} + \frac{1}{\epsilon\rho}H^\varphi - \frac{1}{\epsilon\rho}\frac{\partial H^\rho}{\partial \varphi}. \tag{11}$$

By taking jump values in (11) and noting that $[E^z] = 0$, we have

$$\left[\frac{1}{\epsilon}\frac{\partial H^\varphi}{\partial \rho}\right] + \frac{1}{R}\left[\frac{1}{\epsilon}H^\varphi\right] - \frac{1}{R}\left[\frac{1}{\epsilon}\frac{\partial H^\rho}{\partial \varphi}\right] = 0. \tag{12}$$

All together, we have six jump conditions for local field components (H^ρ, H^φ) [4,39]

$$[H^\rho] = 0, \quad [H^\varphi] = 0, \quad \left[\frac{\partial H^\rho}{\partial \rho}\right] = 0, \quad \left[\frac{\partial H^\rho}{\partial \varphi}\right] = 0, \left[\frac{\partial H^\varphi}{\partial \varphi}\right] = 0, \quad \left[\frac{1}{\epsilon}\frac{\partial H^\varphi}{\partial \rho}\right] + \frac{1}{R}\left[\frac{1}{\epsilon}H^\varphi\right] = \frac{1}{R}\left[\frac{1}{\epsilon}\frac{\partial H^\rho}{\partial \varphi}\right]. \tag{13}$$

In the present study, we will construct novel Cartesian grid methods to solve the full-vectorial eigenvalue problems of H^x and H^y satisfying the Helmholtz Eq. (1) in $\Omega^- \cup \Omega^+$ and subject to the jump conditions (13) on Γ. Since the eigenfunctions decay

exponentially in the cladding, a large enough square computational domain with the Dirichlet zero boundary conditions will be assumed.

2.2. Full-vectorial finite difference methods based on the MIB

We will describe the general procedure of full-vectorial MIB methods in this subsection. Consider a uniform Cartesian grid throughout. To achieve the fourth order of accuracy, the standard fourth order finite difference (FD) discretization of (1) is carried out on grid nodes away from Γ, while the FD weights of nodes in the vicinity of the interface shall be modified. A universal rule here is that to approximate function or its derivatives on one side of interface, one never *directly* refers to function values from the other side. Instead, fictitious values from the other side of the interface will be supplied. For example, we denote H to be either H^x or H^y and $H_{i,j}$ and $\widetilde{H}_{i,j}$ being, respectively, function and fictitious value at the node (x_i, y_j). Referring to Fig. 2(a), we have the following modified FD approximation for the y derivative

$$\frac{\partial^2}{\partial y^2} H_{i,j} = \frac{1}{\Delta y^2}\left(-\frac{1}{12}H_{i,j-2} + \frac{4}{3}H_{i,j-1} - \frac{5}{2}H_{i,j} + \frac{4}{3}\widetilde{H}_{i,j+1} - \frac{1}{12}\widetilde{H}_{i,j+2}\right). \tag{14}$$

This approximation maintains the fourth order of accuracy, provided $\widetilde{H}_{i,j+1}$ and $\widetilde{H}_{i,j+2}$ are accurately estimated. In considering both x and y derivatives, it is sufficient to accurately generate four layers of fictitious values $\widetilde{H}$ (marked with open circles in Fig. 2) surrounding Γ, two inside and two outside. In the MIB schemes, each fictitious value of $\widetilde{H}^x$ and $\widetilde{H}^y$ at a given node (x_i, y_j) will be represented as a linear combination of function values of H^x and H^y on a set of neighboring nodes $\mathbb{S}_{i,j}$

$$\widetilde{H}^x_{i,j} = \sum_{(x_l,y_k)\in\mathbb{S}_{i,j}} \left(A^{i,j}_{l,k}H^x_{l,k} + B^{i,j}_{l,k}H^y_{l,k}\right), \quad \widetilde{H}^y_{i,j} = \sum_{(x_l,y_k)\in\mathbb{S}_{i,j}} \left(C^{i,j}_{l,k}H^x_{l,k} + D^{i,j}_{l,k}H^y_{l,k}\right). \tag{15}$$

The major task of a particular MIB scheme is to determine the points set $\mathbb{S}_{i,j}$ and the representation coefficients $A^{i,j}_{l,k}, B^{i,j}_{l,k}, C^{i,j}_{l,k}$, and $D^{i,j}_{l,k}$ via discretizing jump conditions (13). Finally (15) will be substituted into (14) to modify the y derivative approximation. When all necessary x and y derivatives are corrected in discretizing (1), a matrix equation is generated for solving the fundamental eigenmode of the optical waveguide.

2.3. The MIB interface treatment based on local field components

A key idea in the MIB interface treatment is to decompose the two-dimensional (2D) jump conditions (13) so that they can be imposed in a one-dimensional (1D) manner. For the MIB method reported in [39] which is built based on (H^ρ, H^φ), a detailed discussion of the interface treatment along x direction has been given. Here, we will briefly describe y direction treatment.

Referring to Fig. 2(a), eight fictitious values of $\widetilde{H}^x$ and $\widetilde{H}^y$ on four fictitious points $(x_i, y_{j-1}), (x_i, y_j), (x_i, y_{j+1})$, and (x_i, y_{j+2}) need to be determined. We denote the intersection point of interface Γ and $x = x_i$ grid line as (x_i, Γ_0) and the angle between

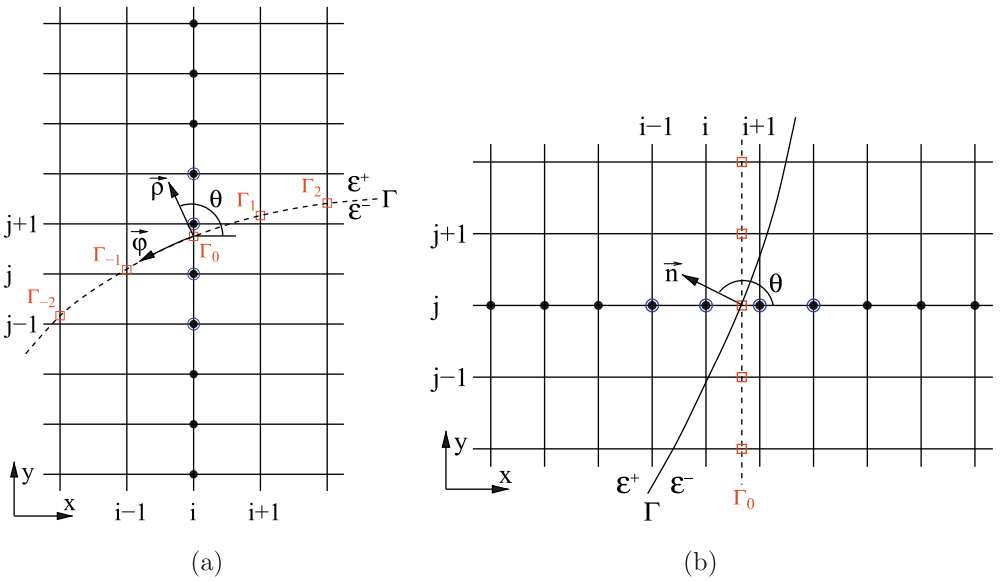

Fig. 2. Illustration of the MIB grid partitions. (a) The MIB scheme based on local field components; (b) The MIB scheme based on global field components. In both cases, the fictitious nodes, original Cartesian nodes, and auxiliary nodes, are shown as, respectively, open circles, filled circles, and squares.

the normal vector at (x_i, Γ_0) and the x-axis as θ. An osculating circle will be formed based on the interface point (x_i, Γ_0) to define a local cylindrical coordinate system $(\vec{\rho}, \vec{\varphi}, \vec{z})$. Coordinate transformations can be employed to convert between the global field components (H^x, H^y) and local components (H^ρ, H^φ)

$$H^\rho = \cos\varphi H^x + \sin\varphi H^y, \quad H^\varphi = -\sin\varphi H^x + \cos\varphi H^y, \tag{16}$$

$$H^x = \cos\varphi H^\rho - \sin\varphi H^\varphi, \quad H^y = \sin\varphi H^\rho + \cos\varphi H^\varphi. \tag{17}$$

With these forward and backward transforms, the task of the MIB interface treatment becomes to represent fictitious values $\widetilde{H}^\rho$ and $\widetilde{H}^\varphi$ on four fictitious points $(x_i, y_{j-1}), (x_i, y_j), (x_i, y_{j+1})$, and (x_i, y_{j+2}) in terms of some nearby H^ρ and H^φ values.

To avoid unnecessary interpolations, jump conditions (13) will be discretized along the y direction using the global Cartesian nodes as shown in Fig. 2(a). We thus need to rewrite jump conditions (13) into Cartesian directions (x, y). Consider H^ρ first. Conditions $\left[\frac{\partial H^\rho}{\partial \rho}\right] = 0$ and $\left[\frac{\partial H^\rho}{\partial \varphi}\right] = 0$ give rise to $\left[\frac{\partial H^\rho}{\partial x}\right] = 0$ and $\left[\frac{\partial H^\rho}{\partial y}\right] = 0$. Consequently, the MIB treatment of H^ρ can be carried out in a 1D manner by discretizing two jump conditions along the y direction

$$[H^\rho] = 0, \quad \left[\frac{\partial H^\rho}{\partial y}\right] = 0. \tag{18}$$

With the details given in [39], the enforcement of (18) yields a representation of four fictitious values $\left(\widetilde{H}^\rho_{i,j-1}, \widetilde{H}^\rho_{ij}, \widetilde{H}^\rho_{i,j+1}, \widetilde{H}^\rho_{i,j+2}\right)^T$ in terms of ten function values $\left(H^\rho_{i,j-4}, H^\rho_{i,j-3}, \ldots, H^\rho_{i,j+5}\right)^T$.

We next consider the MIB treatment for H^φ. Unlike those for H^ρ, jump conditions for H^φ can not be fully decomposed into 1D. To derive necessary equations, we need the transformations for the derivatives

$$\frac{\partial}{\partial \rho} = \cos\varphi \frac{\partial}{\partial x} + \sin\varphi \frac{\partial}{\partial y}, \quad \frac{\partial}{\partial \varphi} = -\rho \sin\varphi \frac{\partial}{\partial x} + \rho \cos\varphi \frac{\partial}{\partial y}. \tag{19}$$

Thus, we have

$$\left[\frac{1}{\epsilon}\frac{\partial H^\varphi}{\partial \rho}\right] = \left[\frac{1}{\epsilon}\cos\varphi \frac{\partial H^\varphi}{\partial x}\right] + \left[\frac{1}{\epsilon}\sin\varphi \frac{\partial H^\varphi}{\partial y}\right] = \cos\theta \left[\frac{1}{\epsilon}\frac{\partial H^\varphi}{\partial x}\right] + \sin\theta \left[\frac{1}{\epsilon}\frac{\partial H^\varphi}{\partial y}\right], \tag{20}$$

$$\left[\frac{1}{\epsilon}\frac{\partial H^\varphi}{\partial \varphi}\right] = -\left[\frac{1}{\epsilon}\rho\sin\varphi \frac{\partial H^\varphi}{\partial x}\right] + \left[\frac{1}{\epsilon}\rho\cos\varphi \frac{\partial H^\varphi}{\partial y}\right] = -R\sin\theta \left[\frac{1}{\epsilon}\frac{\partial H^\varphi}{\partial x}\right] + R\cos\theta \left[\frac{1}{\epsilon}\frac{\partial H^\varphi}{\partial y}\right]. \tag{21}$$

We note that when taking jump values $[\cdot]$, one needs to set $\rho = R$ and $\varphi = \theta$ at the interface point (x_i, Γ_0). According to (20), the last equation in (13) can be rewritten as

$$\cos\theta \left[\frac{1}{\epsilon}\frac{\partial H^\varphi}{\partial x}\right] + \sin\theta \left[\frac{1}{\epsilon}\frac{\partial H^\varphi}{\partial y}\right] + \frac{1}{R}\left[\frac{1}{\epsilon}H^\varphi\right] = \frac{1}{R}\left[\frac{1}{\epsilon}\frac{\partial H^\rho}{\partial \varphi}\right]. \tag{22}$$

By multiplying $R\sin\theta$ on both hand sides of (22), we have

$$R\sin\theta\cos\theta \left[\frac{1}{\epsilon}\frac{\partial H^\varphi}{\partial x}\right] + R\sin^2\theta \left[\frac{1}{\epsilon}\frac{\partial H^\varphi}{\partial y}\right] + \sin\theta \left[\frac{1}{\epsilon}H^\varphi\right] = \sin\theta \left[\frac{1}{\epsilon}\frac{\partial H^\rho}{\partial \varphi}\right]. \tag{23}$$

By substituting (21) to eliminate the x derivative term, one attains

$$R\cos^2\theta \left[\frac{1}{\epsilon}\frac{\partial H^\varphi}{\partial y}\right] - \cos\theta \left[\frac{1}{\epsilon}\frac{\partial H^\varphi}{\partial \varphi}\right] + R\sin^2\theta \left[\frac{1}{\epsilon}\frac{\partial H^\varphi}{\partial y}\right] + \sin\theta \left[\frac{1}{\epsilon}H^\varphi\right] = \sin\theta \left[\frac{1}{\epsilon}\frac{\partial H^\rho}{\partial \varphi}\right]. \tag{24}$$

This simplifies into a first order jump condition involving y and φ derivatives,

$$\left[\frac{1}{\epsilon}\frac{\partial H^\varphi}{\partial y}\right] + \frac{\sin\theta}{R}\left[\frac{1}{\epsilon}H^\varphi\right] = \frac{\cos\theta}{R}\left[\frac{1}{\epsilon}\frac{\partial H^\varphi}{\partial \varphi}\right] + \frac{\sin\theta}{R}\left[\frac{1}{\epsilon}\frac{\partial H^\rho}{\partial \varphi}\right]. \tag{25}$$

We note that the φ derivatives in (25) are continuous across the interface, according to the jump conditions $\left[\frac{\partial H^\rho}{\partial \varphi}\right] = 0$ and $\left[\frac{\partial H^\varphi}{\partial \varphi}\right] = 0$. Thus, the jumps in terms of these two derivatives can be dropped. Therefore, we finally have the following two jump conditions for H^φ

$$[H^\varphi] = 0, \quad \left[\frac{1}{\epsilon}\frac{\partial H^\varphi}{\partial y}\right] + \frac{\sin\theta}{R}\left[\frac{1}{\epsilon}H^\varphi\right] = \frac{\cos\theta}{R}\left(\frac{1}{\epsilon^+} - \frac{1}{\epsilon^-}\right)\frac{\partial H^\varphi}{\partial \varphi} + \frac{\sin\theta}{R}\left(\frac{1}{\epsilon^+} - \frac{1}{\epsilon^-}\right)\frac{\partial H^\rho}{\partial \varphi}. \tag{26}$$

Numerically, two φ derivatives in (26) will be approximated along the arc of the osculating circle. To perform a fourth order FD approximation, a five points stencil sampling at some intersection points of the osculating circle with y grid lines will be employed. For the case shown in Fig. 2(a), these auxiliary points are chosen to be $(x_{i-2}, \Gamma_{-2}), (x_{i-1}, \Gamma_{-1}), (x_i, \Gamma_0), (x_{i+1}, \Gamma_1)$, and (x_{i+2}, Γ_2). After two φ derivatives being accurately estimated, the 1D MIB iterative procedure can be used to discretize jump

conditions (26) along the y direction. This represents four fictitious values $\left(\widetilde{H}^{\varphi}_{i,j-1}, \widetilde{H}^{\varphi}_{ij}, \widetilde{H}^{\varphi}_{i,j+1}, \widetilde{H}^{\varphi}_{i,j+2}\right)^T$ in terms of H^{ρ} and H^{φ} values on ten Cartesian nodes $(x_i, y_{j-4}), (x_i, y_{j-3}), \ldots, (x_i, y_{j+5})$ and five auxiliary points [39].

With representations of $\widetilde{H}^{\rho}$ and $\widetilde{H}^{\varphi}$, the forward and backward transformations (16) and (17) are conducted so that $\widetilde{H}^{x}$ and $\widetilde{H}^{y}$ are now represented by H^x and H^y values on the aforementioned 15 points. Finally, function values of H^x and H^y on each auxiliary point will be interpolated along y line by using five Cartesian nodes exclusively from one side of the interface Γ. Both positive and negative sides can be used in principle. However, for the present study, it has been found that grid nodes from Ω^- give a better result because the eigenfunctions decay exponentially in Ω^+. These interpolations involve additional 20 Cartesian nodes. Together with the 10 Cartesian nodes along the primary y-line, the point set $\mathbb{S}_{ij}$ contains 30 grid nodes. Therefore, in the final MIB discretization, each fictitious value of $\widetilde{H}^{x}$ or $\widetilde{H}^{y}$ will depend on totally 60 function values on these 30 Cartesian nodes [39].

2.4. The MIB interface treatment based on global field components

However, the extension of the MIB method [39] discussed above to deal with arbitrarily curved interfaces can be cumbersome. To carry out all necessary MIB interface treatments, a lot of osculating circles have to be formed throughout the interface. Based on osculating circles, local coordinates need to be established to facilitate forward and backward coordinate transformations. The practical implementation of such a procedure could be tedious. Moreover, there are new mathematical concerns needed to be addressed. For non-constant curvature, the osculating arc only agrees with the interface locally, see Fig. 1(b). When the curvature variants rapidly or when a coarse grid is used, such a mismatching becomes severe and might affect the accuracy of the MIB scheme. Furthermore, for interfaces with negative curvatures or concave segments, the center of the osculating circle will be switched to the positive side of Γ so that the MIB interface matching has to be mathematically reformulated.

We thus propose a new MIB method which is easier to implement. This is essentially achieved via enforcing jump conditions (13) based on global field components H^x and H^y, so that the aforementioned difficulties associated with osculating circles and local coordinates can be bypassed. By using transformation (16), zeroth order jump conditions $[H^{\rho}] = 0$ and $[H^{\varphi}] = 0$ translate into

$$\cos\theta[H^x] + \sin\theta[H^y] = 0, \quad -\sin\theta[H^x] + \cos\theta[H^y] = 0, \tag{27}$$

which further implies $[H^x] = 0$ and $[H^y] = 0$. To derive first order jump conditions, we first completely expand the jump condition $\left[\frac{\partial H^{\rho}}{\partial \rho}\right] = 0$ by using (16) and (19),

$$\cos^2\theta\left[\frac{\partial H^x}{\partial x}\right] + \sin\theta\cos\theta\left[\frac{\partial H^x}{\partial y}\right] + \sin\theta\cos\theta\left[\frac{\partial H^y}{\partial x}\right] + \sin^2\theta\left[\frac{\partial H^y}{\partial y}\right] = 0. \tag{28}$$

Similarly, the full expansion of $\left[\frac{\partial H^{\rho}}{\partial \varphi}\right] = 0$ gives rise to

$$-\sin\theta[H^x] - R\sin\theta\cos\theta\left[\frac{\partial H^x}{\partial x}\right] + R\cos^2\theta\left[\frac{\partial H^x}{\partial y}\right] + \cos\theta[H^y] - R\sin^2\theta\left[\frac{\partial H^y}{\partial x}\right] + R\sin\theta\cos\theta\left[\frac{\partial H^y}{\partial y}\right] = 0. \tag{29}$$

By noting that $[H^x] = 0$ and $[H^y] = 0$, this equation reduces to

$$-\sin\theta\cos\theta\left[\frac{\partial H^x}{\partial x}\right] + \cos^2\theta\left[\frac{\partial H^x}{\partial y}\right] - \sin^2\theta\left[\frac{\partial H^y}{\partial x}\right] + \sin\theta\cos\theta\left[\frac{\partial H^y}{\partial y}\right] = 0. \tag{30}$$

Similarly, the jump condition $\left[\frac{\partial H^{\varphi}}{\partial \varphi}\right] = 0$ will reduce to

$$\sin^2\theta\left[\frac{\partial H^x}{\partial x}\right] - \sin\theta\cos\theta\left[\frac{\partial H^x}{\partial y}\right] - \sin\theta\cos\theta\left[\frac{\partial H^y}{\partial x}\right] + \cos^2\theta\left[\frac{\partial H^y}{\partial y}\right] = 0. \tag{31}$$

Through some algebraic combinations, some simplified jump conditions can be derived:

$$(28)\times\cos\theta - (30)\times\sin\theta: \quad \cos\theta\left[\frac{\partial H^x}{\partial x}\right] + \sin\theta\left[\frac{\partial H^y}{\partial x}\right] = 0, \tag{32}$$

$$(28)\times\sin\theta + (30)\times\cos\theta: \quad \cos\theta\left[\frac{\partial H^x}{\partial y}\right] + \sin\theta\left[\frac{\partial H^y}{\partial y}\right] = 0, \tag{33}$$

$$(30)\times\sin\theta + (31)\times\cos\theta: \quad -\sin\theta\left[\frac{\partial H^y}{\partial x}\right] + \cos\theta\left[\frac{\partial H^y}{\partial y}\right] = 0, \tag{34}$$

$$(30)\times\cos\theta - (31)\times\sin\theta: \quad -\sin\theta\left[\frac{\partial H^x}{\partial x}\right] + \cos\theta\left[\frac{\partial H^x}{\partial y}\right] = 0. \tag{35}$$

Finally, the last equation in (13) can be expanded as

$$\left(-\sin\theta\cos\theta\left[\frac{1}{\epsilon}\frac{\partial H^x}{\partial x}\right]-\sin^2\theta\left[\frac{1}{\epsilon}\frac{\partial H^x}{\partial y}\right]+\cos^2\theta\left[\frac{1}{\epsilon}\frac{\partial H^y}{\partial x}\right]+\sin\theta\cos\theta\left[\frac{1}{\epsilon}\frac{\partial H^y}{\partial y}\right]\right)+\frac{1}{R}\left(-\sin\theta\left[\frac{1}{\epsilon}H^x\right]+\cos\theta\left[\frac{1}{\epsilon}H^y\right]\right)$$
$$=\frac{1}{R}\left(-\sin\theta\left[\frac{1}{\epsilon}H^x\right]-R\sin\theta\cos\theta\left[\frac{1}{\epsilon}\frac{\partial H^x}{\partial x}\right]+R\cos^2\theta\left[\frac{1}{\epsilon}\frac{\partial H^x}{\partial y}\right]+\cos\theta\left[\frac{1}{\epsilon}H^y\right]-R\sin^2\theta\left[\frac{1}{\epsilon}\frac{\partial H^y}{\partial x}\right]+R\sin\theta\cos\theta\left[\frac{1}{\epsilon}\frac{\partial H^y}{\partial y}\right]\right). \tag{36}$$

This gives rise to a simple jump condition

$$\left[\frac{1}{\epsilon}\frac{\partial H^x}{\partial y}\right]=\left[\frac{1}{\epsilon}\frac{\partial H^y}{\partial x}\right], \tag{37}$$

which has been previously studied in the MIB method for rectangular waveguides [38].

The proposed MIB interface treatments employ different sets of jump conditions for x and y-directions. In both cases, the zeroth order jump conditions $[H^x]=0$ and $[H^y]=0$ will be used. For x-direction case, (32) is first chosen. To avoid calculating jump values along y-axis, (37) needs to be rewritten as

$$\left[\frac{1}{\epsilon}\frac{\partial H^y}{\partial x}\right]=\frac{1}{\epsilon^+}\frac{\partial H^{x+}}{\partial y}-\frac{1}{\epsilon^-}\frac{\partial H^{x-}}{\partial y}. \tag{38}$$

For two one-sided limit values in (38) along the y-direction, one will be canceled by using (35) and another will be numerically approximated. In general, one has the freedom to choose the side of cancellation. Nevertheless, for the present study, the positive side will be always canceled because the eigenfunctions are exponentially decaying in Ω^+. This is in consistence with the previous MIB scheme [39]. To this end, (35) is first rewritten as

$$\frac{\partial H^{x+}}{\partial y}=\frac{\partial H^{x-}}{\partial y}+\tan\theta\left[\frac{\partial H^x}{\partial x}\right]. \tag{39}$$

By substituting (39) into (38), one has

$$\left[\frac{1}{\epsilon}\frac{\partial H^y}{\partial x}\right]=\frac{1}{\epsilon^+}\left(\frac{\partial H^{x-}}{\partial y}+\tan\theta\left[\frac{\partial H^x}{\partial x}\right]\right)-\frac{1}{\epsilon^-}\frac{\partial H^{x-}}{\partial y}. \tag{40}$$

Therefore, the MIB interface treatment along x-direction is based on the following four jump conditions

$$[H^x]=0,\quad [H^y]=0,\quad \cos\theta\left[\frac{\partial H^x}{\partial x}\right]+\sin\theta\left[\frac{\partial H^y}{\partial x}\right]=0,\quad \left[\frac{1}{\epsilon}\frac{\partial H^y}{\partial x}\right]-\frac{\tan\theta}{\epsilon^+}\left[\frac{\partial H^x}{\partial x}\right]=\left(\frac{1}{\epsilon^+}-\frac{1}{\epsilon^-}\right)\frac{\partial H^{x-}}{\partial y}. \tag{41}$$

Through similar derivation, the MIB interface treatment along y-direction is based on the following four jump conditions

$$[H^x]=0,\quad [H^y]=0,\quad \cos\theta\left[\frac{\partial H^x}{\partial y}\right]+\sin\theta\left[\frac{\partial H^y}{\partial y}\right]=0,\quad \left[\frac{1}{\epsilon}\frac{\partial H^x}{\partial y}\right]-\frac{\cot\theta}{\epsilon^+}\left[\frac{\partial H^y}{\partial y}\right]=\left(\frac{1}{\epsilon^+}-\frac{1}{\epsilon^-}\right)\frac{\partial H^{y-}}{\partial x}. \tag{42}$$

2.5. The MIB discretization of jump conditions

The MIB discretization of jump conditions (41) will be discussed in this subsection, while the y direction MIB scheme for (42) can be similarly constructed. Consider a grid configuration as shown in Fig. 2(b). Denote the angle between x direction and the outward normal vector $\vec{n}$ at the interface point (Γ_0, y_j) to be θ. The FD approximation at (x_{i+1}, y_j) will be modified to be

$$\frac{\partial^2}{\partial x^2}H_{i+1,j}=\frac{1}{\Delta x^2}\left(-\frac{1}{12}\widetilde{H}_{i-1,j}+\frac{4}{3}\widetilde{H}_{ij}-\frac{5}{2}H_{i+1,j}+\frac{4}{3}H_{i+2,j}-\frac{1}{12}H_{i+3,j}\right). \tag{43}$$

An iterative procedure is commonly employed in the MIB schemes [40,42,41,38,39] to determine all necessary fictitious values.

At the first step, we determine four fictitious values $\left(\widetilde{H}^x_{ij}, \widetilde{H}^y_{ij}, \widetilde{H}^x_{i+1,j}, \widetilde{H}^y_{i+1,j}\right)$ by discretizing four jump conditions (41) in the same manner of (43). In particular, we define two grid stencils along the primary line $y=y_j$, i.e., $\mathbf{H}_x^- := (H^x_{i-4,j}, H^x_{i-3,j}, H^x_{i-2,j}, H^x_{i-1,j}, H^x_{ij}, \widetilde{H}^x_{i+1,j})^T$ and $\mathbf{H}_x^+ := (\widetilde{H}^x_{ij}, H^x_{i+1,j}, H^x_{i+2,j}, H^x_{i+3,j}, H^x_{i+4,j}, H^x_{i+5,j})^T$. Also, $\mathbf{H}_y^-$ and $\mathbf{H}_y^+$ can be defined similarly. Denote the finite difference (FD) weight vector of these two stencils differentiating at Γ_0 to be, respectively, $\mathbf{W}_k^-$ and $\mathbf{W}_k^+$. Here the subscript k represents interpolation ($k=0$) and the first order derivative approximation ($k=1$). With these FD weights, the first three jump conditions in (41) can be discretized as

$$\mathbf{W}_0^-\mathbf{H}_x^- = \mathbf{W}_0^+\mathbf{H}_x^+,\quad \mathbf{W}_0^-\mathbf{H}_y^- = \mathbf{W}_0^+\mathbf{H}_y^+,\ \cos\theta\mathbf{W}_1^-\mathbf{H}_x^- + \sin\theta\mathbf{W}_1^-\mathbf{H}_y^- = \cos\theta\mathbf{W}_1^+\mathbf{H}_x^+ + \sin\theta\mathbf{W}_1^+\mathbf{H}_y^+. \tag{44}$$

The last jump condition in (41) involves one y derivative, which has to be approximated along the y direction. Denote some auxiliary points to be intersection points of the line $x=\Gamma_0$ with y grid lines, i.e., $(\Gamma_0, y_{j-2}), (\Gamma_0, y_{j-1}), (\Gamma_0, y_j), (\Gamma_0, y_{j+1})$, and

(Γ_0, y_{j+2}) in Fig. 2(b). Let the H^{x-} values on these five auxiliary nodes be $\mathbf{H}_x^{\Gamma} := (H^{x-}_{\Gamma_0,j-2}, H^{x-}_{\Gamma_0,j-1}, H^{x-}_{\Gamma_0,j}, H^{x-}_{\Gamma_0,j+1}, H^{x-}_{\Gamma_0,j+2})^T$ and the corresponding FD weights differentiating at (Γ_0, y_j) to be $\mathbf{W}_k^{\Gamma}$. Then the last condition in (41) is discretized to be

$$\frac{1}{\epsilon^+}\mathbf{W}_1^+\mathbf{H}_y^+ - \frac{\tan\theta}{\epsilon^+}\mathbf{W}_1^+\mathbf{H}_x^+ = \frac{1}{\epsilon^-}\mathbf{W}_1^-\mathbf{H}_y^- - \frac{\tan\theta}{\epsilon^+}\mathbf{W}_1^-\mathbf{H}_x^- + \left(\frac{1}{\epsilon^+} - \frac{1}{\epsilon^-}\right)\mathbf{W}_1^{\Gamma}\mathbf{H}_x^{\Gamma}. \tag{45}$$

By solving four linear algebraic equations given in (44) and (45), one attains four fictitious values $\left(\widetilde{H}^x_{i,j}, \widetilde{H}^y_{i,j}, \widetilde{H}^x_{i+1,j}, \widetilde{H}^y_{i+1,j}\right)$.

Another four fictitious values can be determined by repeating the above procedure on augmented stencils. In particular, one more fictitious node will be added in $\mathbf{H}_x^-, \mathbf{H}_x^+, \mathbf{H}_y^-$, and $\mathbf{H}_y^+$. For example, now $\mathbf{H}_y^-$ and $\mathbf{H}_y^+$ are updated to be $\mathbf{H}_y^- := \left(H^y_{i-4,j}, \ldots, H^y_{i,j}, \widetilde{H}^y_{i+1,j}, \widetilde{H}^y_{i+2,j}\right)^T$ and $\mathbf{H}_y^+ := \left(\widetilde{H}^y_{i-1,j}, \widetilde{H}^y_{i,j}, H^y_{i+1,j}, \ldots, H^x_{i+5,j}\right)^T$, while $\mathbf{H}_x^-$ and $\mathbf{H}_x^+$ are similarly re-defined. Consequently, the FD weights $\mathbf{W}_k^-$ and $\mathbf{W}_k^+$ need to be re-calculated too. With these new notations, four linear algebraic equations in (44) and (45) will be solved again to deliver four fictitious values $\left(\widetilde{H}^x_{i-1,j}, \widetilde{H}^y_{i-1,j}, \widetilde{H}^x_{i+2,j}, \widetilde{H}^y_{i+2,j}\right)$.

The MIB scheme discussed above will essentially represent four layers of $\widetilde{H}^x$ and $\widetilde{H}^y$ in terms of H^x and H^y values on ten Cartesian nodes $(x_{i-4}, y_j), (x_{i-3}, y_j), \ldots, (x_{i+5}, y_j)$ and H^{x-} values on five auxiliary nodes. As in [39], these auxiliary values will be interpolated/extrapolated along x line by using five nearest nodes exclusively from one side of the interface. Here, we will only use on-grid H^x values from Ω^-, as H^{x-} in Eq. (41) is defined for the negative side. Numerically speaking, such an approximation could be an interpolation or an extrapolation. For example, referring to the Fig. 2(b), to estimate $H^{x-}_{\Gamma_0,j-2}$ the interpolation stencil consists of grid points $(i, j-2)$ to $(i+4, j-2)$, while to approximate $H^{x-}_{\Gamma_0,j+1}$ the extrapolation stencil consists of grid points $(i+2, j+1)$ to $(i+6, j+1)$. After interpolation/extrapolation, the size of the point set $\mathbb{S}$ remains to be 30 as in [39]. However, since only H^x values are required on 20 nodes that are not along the primary line $y = y_i$, only 40 function values of H^x and H^y are needed to represent each fictitious value of $\widetilde{H}^x$ or $\widetilde{H}^y$. This implies a smaller matrix bandwidth, comparing with the previous MIB scheme [39]. Of course, such a bandwidth is still much larger than the regular FD discretization. Nevertheless, even though such a bandwidth slightly increases the computing time of the iterative eigenvalue solver, the MIB scheme is still cost-effective in sense that a coarse mesh is sufficient to achieve high accuracy [38].

3. Numerical experiments

The benchmark tests of step-index fibers [23,18] are considered first to validate the proposed full-vectorial MIB approach. The fourth order convergence has been numerically confirmed when applying the previously developed MIB method [39] to these tests. Because the dielectric interface is a circle, the previous MIB method [39] which is based on the cylindrical components (H^ρ, H^φ) is obviously well suited to the problem. In this work, it is of great interest to investigate the performance of the new MIB method based on the Cartesian components (H^x, H^y).

As in [23,18,39], three fiber cases are considered with the fixed core radius $R = 4$ μm. Denote the refractive index for the core and cladding to be respectively, n_{core} and n_{clad}. The model parameters $(n_{\text{core}}, n_{\text{clad}}, \lambda)$ are chosen as, respectively, (1.45, 1.44, 1.55), (1.5, 1.0, 6.2), and (3.5, 1.0, 6.2) in Cases 1, 2, and 3. An iterative eigenvalue solver based on the simultaneous iteration method [2] is used to determine the fundamental HE_{11} mode. As in [39], a large enough square computational domain $[-a, a] \times [-a, a]$ is employed with Dirichlet zero boundary conditions being prescribed on boundaries. A uniform mesh with size $N \times N$ or $\Delta x = \Delta y$ is employed. The geometrical symmetry of the waveguide structure is usually exploited in literature [18] by discretizing only one-quarter of the domain. In the present study, the entire domain will be discretized, because we are interested in testing the MIB method in dealing with interfaces with arbitrary orientation and location with respect to the Cartesian coordinate. Also, non-integer domain dimension a will be used. In particular, a is selected to be $10 + \pi/3$ for Cases 1 and 2, and $5 + \pi/3$ for Case 3.

The absolute errors in effective propagation constants $\beta_e = \beta/\omega$ are computed against the analytical solutions [23,18,39] and are depicted as dashed lines in Fig. 3. A linear fitting by means of the least squares is then conducted in the log–log scale

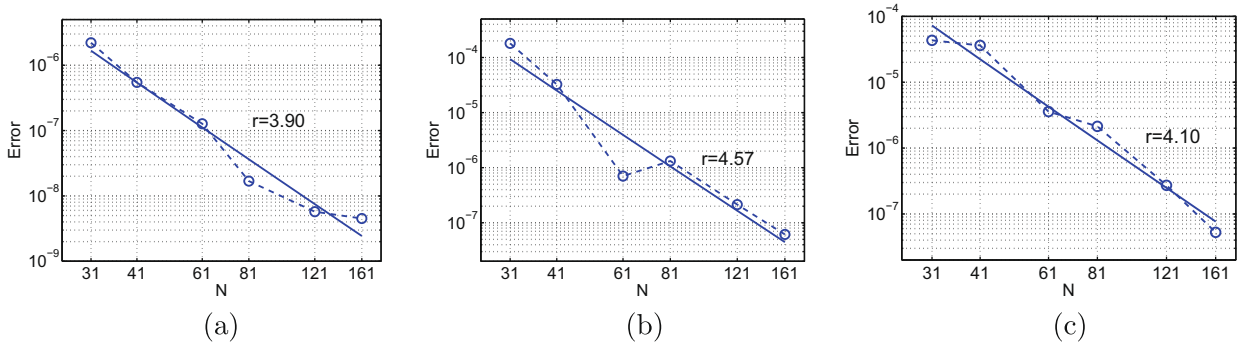

Fig. 3. Numerical convergence tests of the MIB scheme for constant curvature problems. (a) Case 1; (b) Case 2; (c) Case 3.

[38,39]. This essentially yields the numerical convergence rate r of the MIB scheme. For Cases 1, 2, and 3, the numerical order r is calculated to be 3.90, 4.57, and 4.10. These r values and corresponding solid convergence lines are also shown in Fig. 3. It is clear that the proposed MIB scheme achieves the fourth order convergence for dielectric interfaces with constant curvature.

We next explore the performance of the proposed MIB method for interfaces with non-constant curvatures. To this end, the following interface which is parameterized with the polar angle s will be studied

$$\Gamma: \quad \sqrt{x^2+y^2} = \frac{1}{2} + b\sin(ms), \quad s \in [0, 2\pi]. \tag{46}$$

Here the parameter m determines the number of "leaves" of the core region and b controls the magnitude of the curvature. Four independent tests with parameters $(m,b) = (2,1/4), (3,1/8), (4,1/8)$, and $(5,1/10)$, are considered. The resulting configurations are shown on the right upper corner of each chart of Fig. 4. It is clear that concave segments or negative curvatures are involved in the present interfaces. In all four cases, we will fix the wavelength $\lambda = 0.5$ and step-index profile to be $n_{\text{core}} = 3.5$ and $n_{\text{clad}} = 1$. As in the previous studies, we will assume a large enough computational domain $[-a,a] \times [-a,a]$ and a uniform mesh with size $N \times N$. Here we choose $a = \pi/3$. No analytical solution is available for the present waveguides with arbitrarily curved interfaces. To benchmark our numerical results, for each case, an "exact" solution is computed by using the MIB method based on a very dense mesh. In particular, the exact effective propagation constant is estimated to be $\beta_e = 3.47464791 \pm 4 \times 10^{-8}, \beta_e = 3.47680822 \pm 4 \times 10^{-8}, |\beta_e| = 3.47554731 \pm 1 \times 10^{-8}$, and $\beta_e = 3.47653400 \pm 1 \times 10^{-8}$, respectively, for Cases 1, 2, 3, and 4.

By comparing with the exact values, the MIB errors and corresponding convergence lines are depicted in Fig. 4. These results clearly indicate that the MIB method achieves the fourth order convergence for interfaces with non-constant curvatures. On the other hand, it can be observed from Fig. 4 that when the geometrical structure becomes more complicated or the number of leaves m increases, the convergence pattern of the MIB method becomes more oscillatory and the numer-

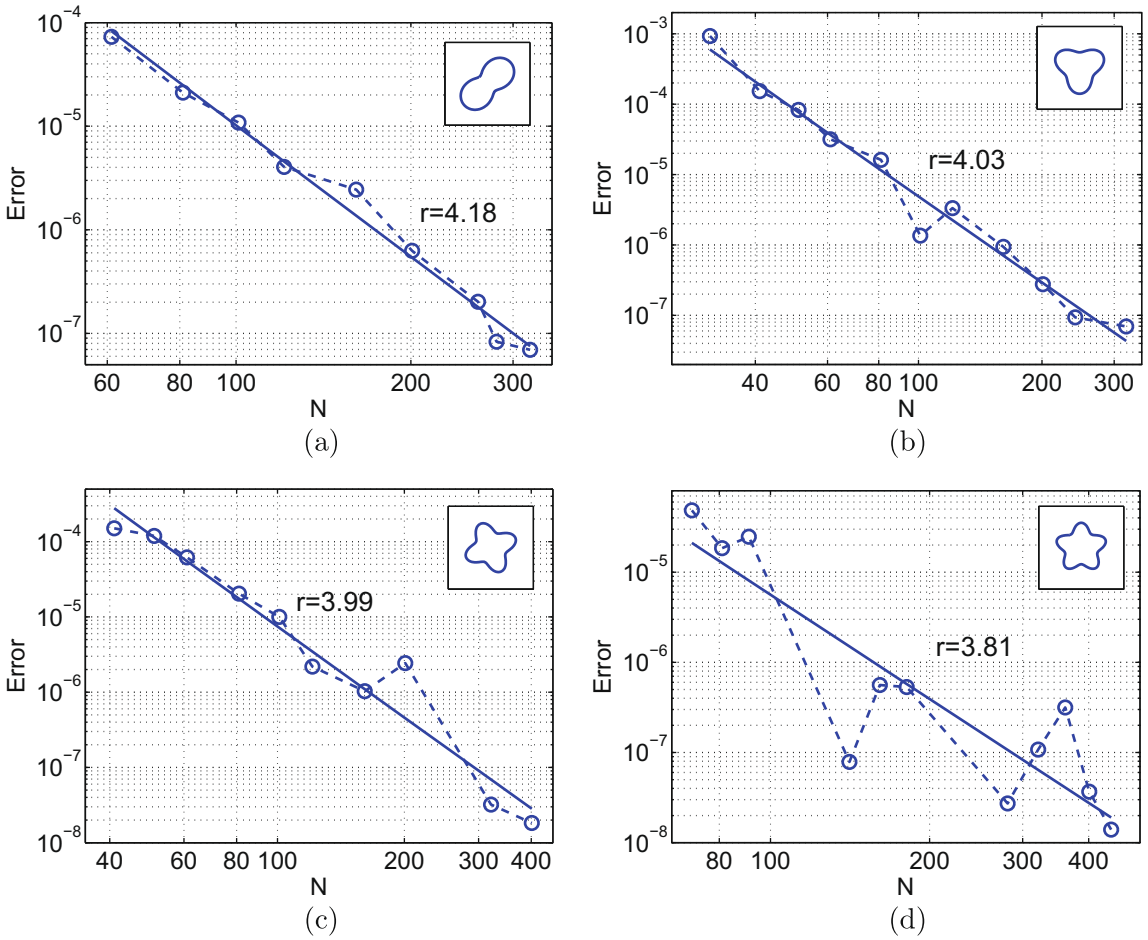

Fig. 4. Numerical convergence tests of the MIB scheme for non-constant curvature problems. (a) Case 1, $(m,b) = (2,1/4)$; (b) Case 2, $(m,b) = (3,1/8)$; (c) Case 3, $(m,b) = (4,1/8)$; (c) Case 4, $(m,b) = (5,1/10)$.

ically detected order becomes slightly smaller. This should be due to the complex nature of the eigenmodes induced by the structure.

To gain an in-depth understanding, we depict the eigenfunctions of the fundamental modes for all four cases in Figs. 5–8. Both mesh plots and contour plots are presented. In all contour plots, the corresponding dielectric interface is shown as a dashed line. We have the following interesting observations from these figures. First, in all charts, eigenmodes are well confined within the interface. This is because of the fast decay of eigenfunctions in the cladding. Second, in comparing among four cases, certain dependence of field pattern on the integer m can be observed. For even integers, i.e., Cases 1 and 3, both H^x and H^y are non-oscillatory or can be described as single modes. However, for odd integers, i.e., Cases 2 and 4, the dominant field H^y remains to be single mode, while the minor field H^x is oscillatory or involves multimodes. The appearance of these multimodes in H^x shall be due to the fact that the waveguide structure is less symmetrical for odd leaves than for even leaves. Third, a very complicated multimode pattern is observed for H^x in the Case 4, see Fig. 8(c). It is well known that the accurate simulation of high frequency wave is numerically very challenging, especially when this is coupled with field discontinuities across arbitrarily curved interfaces. It is believed that the highly non-uniform convergence trend of the MIB method shown in Fig. 4(d) is caused by these issues. However, the overall order of accuracy of the proposed MIB method remains to be four in this very challenging test. This demonstrates the robustness of the MIB method in resolving optical waveguides with arbitrarily curved interfaces.

Finally, we note that the fundamental eigenvalues and eigenfunctions of the Case 3 are complex, while those of the other three cases are real. In fact, the absolute value $|\beta_e|$ instead of β_e is reported for the Case 3 in Fig. 4. The exact physical reasoning of this complex mode is not very clear. It is perhaps because of the fourfold rotational symmetry of this Case. One thing which we can certain is that the complex nature is essential to this four leaves structure. To illustrate this point, we consider a rotation of the structure by introducing a phase angle t in the interface profile:

$$\Gamma: \quad \sqrt{x^2+y^2} = \frac{1}{2} + \frac{1}{8}\sin(4(s+t)), \quad s \in [0, 2\pi]. \tag{47}$$

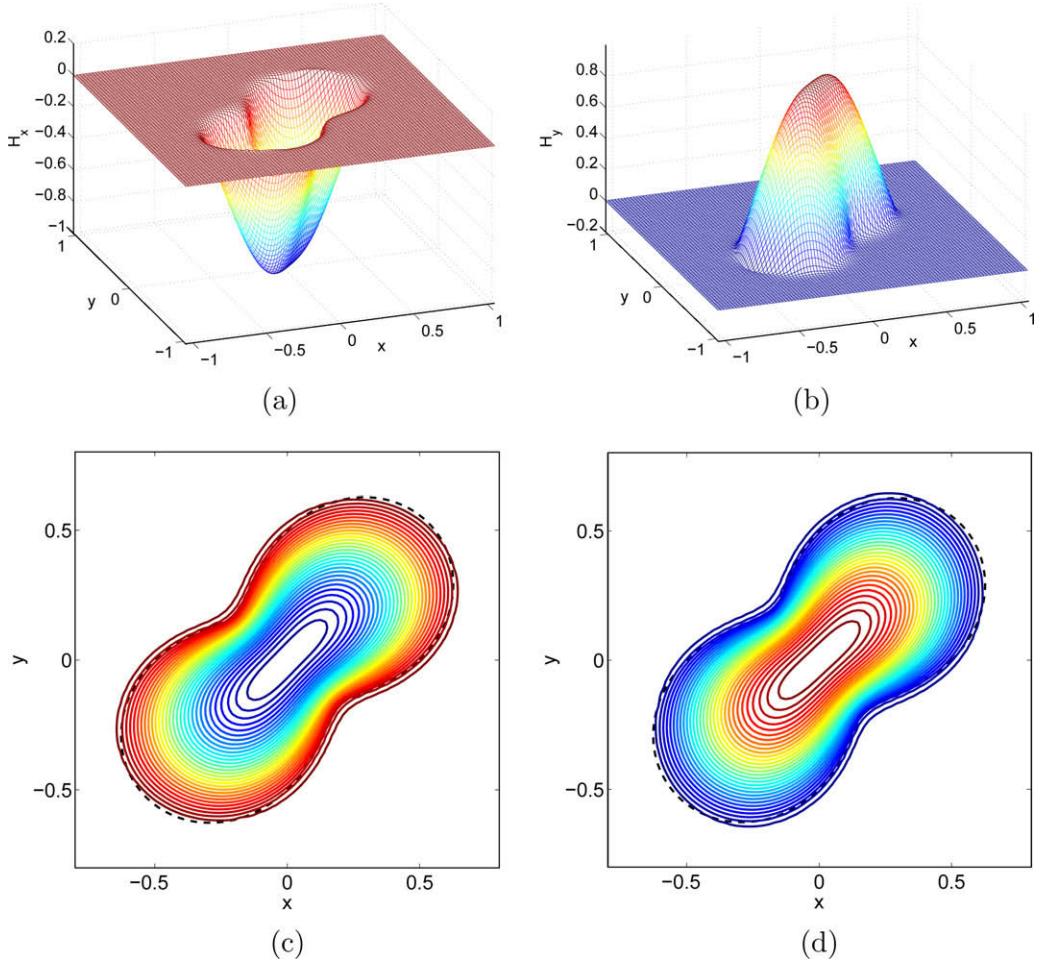

Fig. 5. The fundamental modes in the Case 1. (a) H^x. (b) H^y. (c) Contour plot of H^x. (d) Contour plot of H^y.

By using a fixed mesh size with $N = 121$, several rotational angles are tested within $t \in [0, \frac{\pi}{2})$. The corresponding fundamental eigenvalues are all complex, see Table 1. We note that by using a fixed computational domain $[-\pi/3, \pi/3] \times [-\pi/3, \pi/3]$ and the Dirichlet zero boundary conditions in different orientations, the numerical modes are of course different, even though the shape of the structure is invariant. The differences between the rotated modes and the unrotated mode are listed in the last column of Table 1. On the other hand, it is noted that the numerical error of the unrotated mode with $N = 121$ is about 2.42×10^{-6}, see also Fig. 4(c). Obviously, the differences shown in Table 1 are all within the order of the numerical error of the unrotated mode. For this reason, it is believed that given a large enough computational domain, the numerical eigenvalues of the rotated modes will also converge to the same limit value of the unrotated mode – that is the physical

Table 1
Fundamental modes for different orientations of the four leaves structure.

Phase t_i	$Re(\beta_e^{t_i})$	$Im(\beta_e^{t_i})$	$\lvert\beta_e^{t_i} - \beta_e^{t_0}\rvert$
$t_0 = 0$	3.4755494992	1.05×10^{-6}	
$t_1 = \frac{\pi}{8}$	3.4755523185	6.28×10^{-7}	2.85×10^{-6}
$t_2 = \frac{\pi}{7}$	3.4755531302	8.74×10^{-7}	3.64×10^{-6}
$t_3 = \frac{\pi}{6}$	3.4755543737	5.66×10^{-7}	4.90×10^{-6}
$t_4 = \frac{\pi}{5}$	3.4755551534	2.16×10^{-7}	5.72×10^{-6}
$t_5 = \frac{\pi}{4}$	3.4755494992	1.05×10^{-6}	3.19×10^{-13}
$t_6 = \frac{\pi}{3}$	3.4755523787	1.12×10^{-7}	3.03×10^{-6}

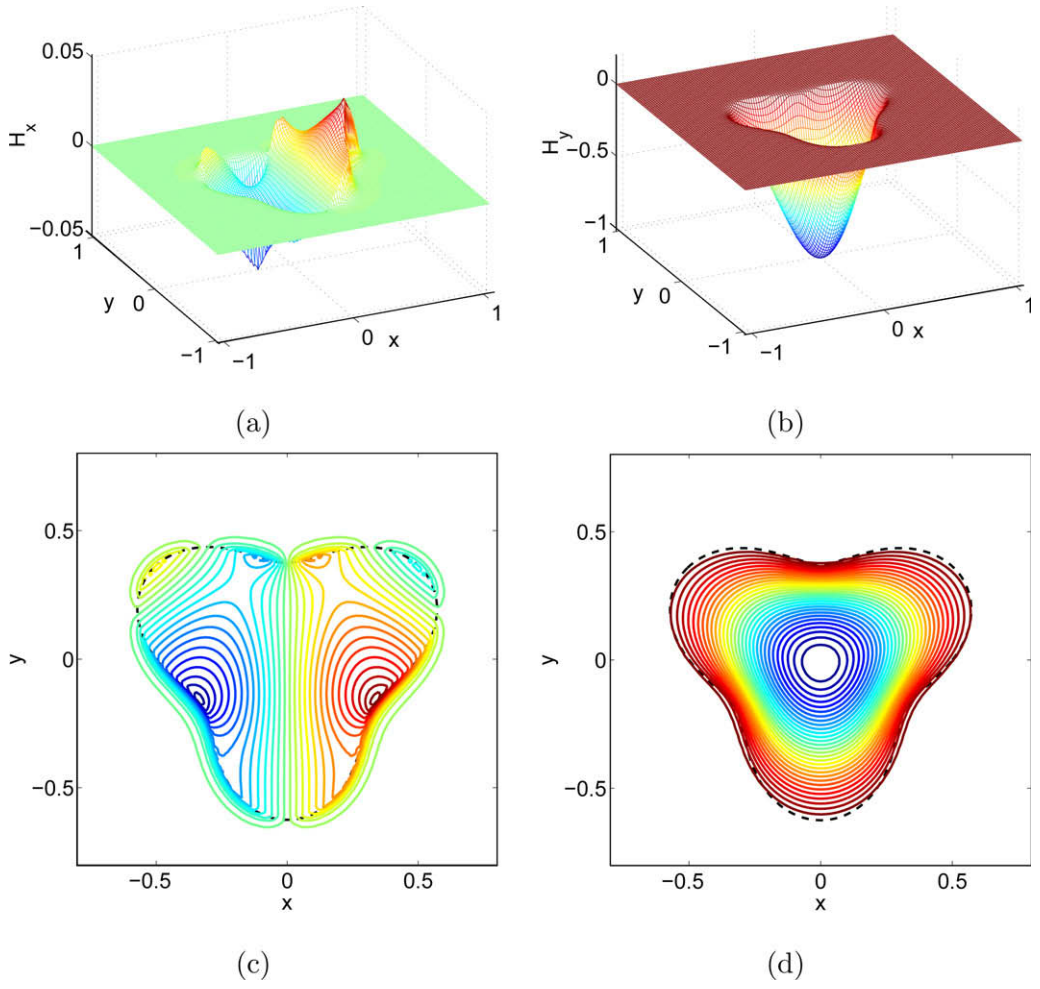

Fig. 6. The fundamental modes in the Case 2. (a) H^x. (b) H^y. (c) Contour plot of H^x. (d) Contour plot of H^y.

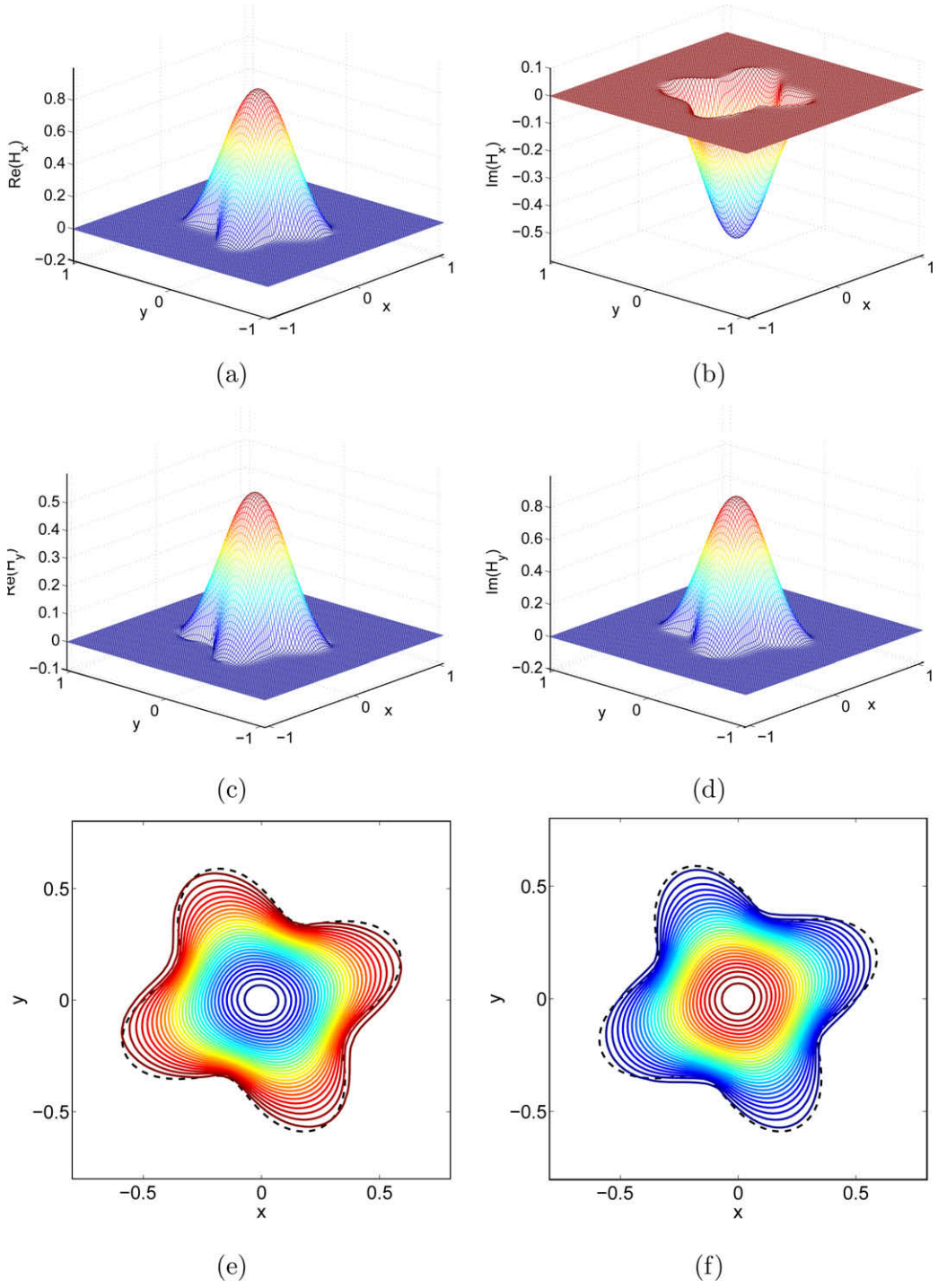

Fig. 7. The fundamental modes in the Case 3. (a) The real part of H^x. (b) The imaginary part of H^x. (c) The real part of H^y. (d) The imaginary part of H^y. (e) Contour plot of the imaginary part of H^x. (f) Contour plot of the imaginary part of H^y.

mode corresponding to this four leaves structure. At last, we note that the imaginary parts of the fundamental models $\mathrm{Im}(\beta_e)$ for all orientations are actually very small. When computing magnitude or absolute value $|\beta_e|$, the contribution from the imaginary parts is comparable to the double precision limit, and is thus negligible.

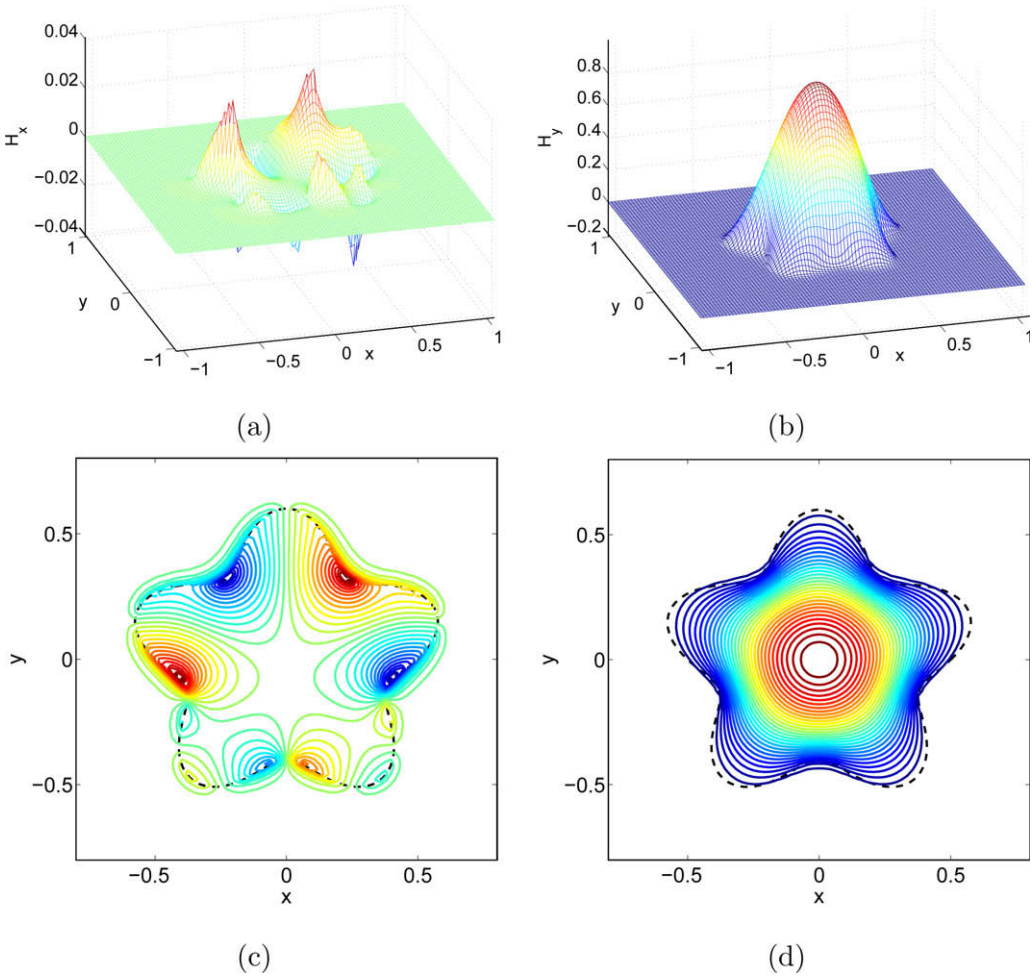

Fig. 8. The fundamental modes in the Case 4. (a) H^x. (b) H^y. (c) Contour plot of H^x. (d) Contour plot of H^y.

Table 2
Numerically detected CPU times for the optical fiber test (measured in second).

	Case 1		Case 2		Case 3	
N	MIB	Total	MIB	Total	MIB	Total
31	0.071	1.078	0.072	1.041	0.118	4.090
61	0.163	25.922	0.135	9.028	0.240	48.033
121	0.301	368.095	0.265	219.999	0.484	935.971

4. Concluding remarks

This paper overcomes the difficulty of the previous matched interface and boundary (MIB) method [39] in dealing with interfaces with non-constant curvatures for optical waveguide analysis. A novel full-vectorial MIB method is formulated for transverse components of the magnetic field **H**. Without introducing local cylindrical coordinates, the MIB interface treatments are conducted along Cartesian directions, based on the newly derived jump conditions. In comparing with the previous MIB method [39], the proposed MIB method involves a smaller bandwidth for grid nodes in the vicinity of the interface and its numerical implementation is relatively easier. The fourth order convergence of the proposed MIB method is numerically confirmed for benchmark optical fiber problems. In dealing with more challenging waveguide structures with arbitrarily curved interfaces, the MIB method still achieves the fourth order of accuracy, even in cases where high frequency solutions are interacted with the material interfaces. The generalization of the MIB method to time domain problems are under our consideration. We finally note the following two features of the MIB method:

- Both the present MIB and the previous MIB [39] are designed for smoothly curved interfaces, i.e., C^1 continuous interfaces. The fourth order convergence can not be guaranteed if the interface is only C^0 continuous, because certain corner singularity problems may occur [17,29,38].
- Computationally speaking, the CPU time spend for the MIB preprocessing is usually much less than that costed by solving the eigenvalues via a standard iterative solver [2]. As discussed above, the bandwidth of the MIB method for each irregular node is fixed to be 40 in the present MIB method. Moreover, such a bandwidth is independent of the mesh size N. On the other hand, the total number of irregular nodes increases with respect to the mesh size N linearly, because the number of total irregular points is one-dimension lower than the number of total grid points. Thus, the computational overhead of the MIB treatments essentially scales as $O(N)$. Furthermore, the MIB treatment of a single irregular node is actually very efficient. The major algebraic computation is solving a small linear system, such as (44) and (45), to attain representation coefficients. Therefore, the CPU time for MIB preprocessing is usually negligible in practical computations. To illustrate this point, the numerically detected CPU times for the three cases of optical fiber test are listed in Table 2. The linear trend is clearly seen for the MIB CPU times for all three cases and the MIB overhead costs less than 1% CPU time when N is large.

Acknowledgments

This work was supported in part by the NSF under Grants DMS-0616704 and DMS-0731503.

References

[1] A.P. Ansbro, I. Montrosset, Vectorial finite difference scheme for isotropic dielectric waveguides: transverse electric filed representation, IEE Proc. Part J. Optoelectron. 140 (1993) 253–259.
[2] Z. Bai, G.W. Stewart, SRRIT: A Fortran subroutine to calculate the dominant invariant subspace of a nonsymmetric matrix, ACM Trans. Math. Software 23 (1997) 494–513.
[3] P.-J. Chiang, C.-L. Wu, C.-H. Teng, C.-S. Yang, H.-C. Chang, Full-vectorial optical waveguide mode solvers using multidomain pseudospectral frequency-domain (PSFD) formulations, IEEE J. Quant. Electron. 44 (2008) 56–66.
[4] Y.C. Chiang, Y.P. Chiou, H.C. Chang, Improved full-vectorial finite-difference mode solver for optical waveguides with step-index profiles, J. Lightwave Technol. 20 (2002) 1609–1618.
[5] Y.P. Chiou, Y.C. Chiang, H.C. Chang, Improved three-point formulas considering the interface conditions in the finite-difference analysis of step-index optical devices, J. Lightwave Technol. 18 (2000) 243–251.
[6] S. Cogollos, S. Marini, V.E. Boria, P. Soto, A. Vidal, H. Esteban, J.V. Morro, B. Gimeno, Efficient model analysis of arbitrarily shaped waveguides composed of linear, circular, and elliptical arcs using the BI-RME method, IEEE Trans. Micro. Theory Technol. 51 (2003) 2378–2390.
[7] K. Dossou, M. Fontaine, A high order isoparametric finite element method for the computation of waveguide modes, Comput. Methods Appl. Mech. Engrg. 194 (2005) 837–858.
[8] K. Fan, W. Cai, X. Ji, A full vectorial generalized discontinuous Galerkin beam propagation method (GDG-BPM) for nonsmooth electromagnetic fields in waveguides, J. Comput. Phys. 227 (2008) 7178–7191.
[9] R.P. Fedkiw, T. Aslam, B. Merriman, S. Osher, A non-oscillatory Eulerian approach to interfaces in multimaterial flows (the ghost fluid method), J. Comput. Phys. 152 (1999) 457–492.
[10] F. Gibou, R.P. Fedkiw, L.-T. Cheng, M. Kang, A second-order-accurate symmetric discretization of the Poisson equation on irregular domain, J. Comput. Phys. 176 (2002) 205–227.
[11] F. Gibou, R.P. Fedkiw, A forth order accurate discretization for the Laplace and heat equations on arbitrary domains, with applications to the Stefan problem, J. Comput. Phys. 202 (2005) 577–601.
[12] H.A. Jamid, M.N. Akram, A new higher order finite-difference approximation scheme for the method of lines, J. Lightwave Technol. 19-3 (2001) 398–404.
[13] G.R. Hadley, R.E. Smith, Full-vector waveguide modeling using an iterative finite-difference method with transparent boundary conditions, J. Lightwave Technol. 13 (1995) 465–469.
[14] G.R. Hadley, Low-truncation-error finite difference equations for photonics simulation I: beam propagation, J. Lightwave Technol. 16-1 (1998) 134–141.
[15] G.R. Hadley, Low-truncation-error finite difference equations for photonics simulation II: vertical-cavity surface-emitting lasers, J. Lightwave Technol. 16-1 (1998) 142–151.
[16] G.R. Hadley, High-accuracy finite-difference equations for dielectric waveguide analysis I: uniform regions and dielectric interfaces, J. Lightwave Technol. 20-7 (2002) 1210–1218.
[17] G.R. Hadley, High-accuracy finite-difference equations for dielectric waveguide analysis II: dielectric corners, J. Lightwave Technol. 20-7 (2002) 1219–1231.
[18] G.R. Hadley, Numerical simulation of waveguides of arbitrary cross-section, Int. J. Electron. Common. 58 (2004) 86–92.
[19] M. Koshiba, Optical Waveguide Theory by the Finite Element Method, Kluwer, Norwell, MA, 1992.
[20] M. Koshiba, Y. Tsuji, Curvilinear hybrid edge/nodal elements with triangular shape for guide-wave problems, J. Lightwave Technol. 18 (2000) 737–743.
[21] R.J. LeVeque, Z.L. Li, The immersed interface method for elliptic equations with discontinuous coefficients and singular sources, SIAM J. Numer. Anal. 31 (1994) 1019–1044.
[22] X.D. Liu, R.P. Fedkiw, M. Kang, A boundary condition capturing method for Poisson's equation on irregular domains, J. Comput. Phys. 160 (2000) 151–178.
[23] T. Lu, D. Yevick, A vectorial boundary element method analysis of integrated optical waveguides, J. Lightwave Technol. 21 (2003) 1793–1807.
[24] P. Lüsse, P. Stuwe, J. Schüle, H.-G. Unger, Analysis of vectorial mode fields in optical waveguides by a new finite difference method, J. Lightwave Technol. 12 (1994) 487–494.
[25] Y.T. Ng, H. Chen, C. Min, F. Gibou, Guidelines for Poisson solvers on irregular domains with Dirichlet boundary conditions using the ghost fluid method, J. Sci. Comput. 41 (2009) 300–320.
[26] M.J. Robertson, S. Ritchie, P. Dayan, Semiconductor waveguides: analysis of optical propagation in single rib structures and directional couplers, IEE Proc. Part J. Optoelectron. 132 (1985) 336–342.
[27] M.S. Stern, Semivectorial polarised finite difference method for optical waveguides with arbitrarily index profiles, IEE Proc. Part J. Optoelectron. 135 (1988) 56–63.
[28] R. Stoffer, H.J.W.M. Hoekstra, Efficient interface conditions based on a 5-point finite difference operator, Opt. Quant. Electron. 30 (1998) 375–383.

[29] N. Thomas, P. Sewell, T.M. Benson, A new full-vectorial higher order finite-difference scheme for the modal analysis of rectangular dielectric waveguides, J. Lightwave Technol. 25 (2007) 2563–2570.
[30] A.K. Tornberg, B. Engquist, Numerical approximations of singular source terms in differential equations, J. Comput. Phys. 200 (2004) 462–488.
[31] C. Vassallo, Improvement of finite difference methods for step-index optical waveguides, IEE Proc. Part J. Optoelectron. 139 (1992) 137–142.
[32] C. Vassallo, Interest of improved three-point formulas for finite-difference modeling of optical devices, J. Opt. Soc. Am. A 14-12 (1997) 3273–3284.
[33] J.S. Xia, J.Z. Yu, New finite-difference scheme for simulations of step-index waveguides with tilt interfaces, IEEE Photon. Technol. Lett. 15-9 (2003) 1237–1239.
[34] C.L. Xu, W.P. Huang, M.S. Stern, S.K. Chaudhuri, Full-vectorial mode calculations by finite difference method, IEE Proc. Part J. Optoelectron. 141 (1994) 281–286.
[35] J. Yamauchi, T. Murata, H. Nakano, Semivectorial H-field analysis of rib waveguides by a modified beam-propagation method based on the generalized Douglas scheme, Opt. Lett. 25-24 (2000) 1171–1173.
[36] W.D. Yang, R. Pregla, The method of lines for analysis of integrated optical waveguide structures with arbitrary curved interfaces, J. Lightwave Technol. 14 (1996) 879–884.
[37] S. Zhao, On the spurious solutions in the high-order finite difference methods, Comput. Methods Appl. Mech. Engrg. 196 (2007) 5031–5046.
[38] S. Zhao, Full-vectorial matched interface and boundary (MIB) method for the modal analysis of dielectric waveguides, J. Lightwave Technol. 26 (2008) 2251–2259.
[39] S. Zhao, High order vectorial analysis of waveguides with curved dielectric interfaces, IEEE Microwave Compon. Lett. 19 (2009) 266–268.
[40] S. Zhao, G.W. Wei, High-order FDTD methods via derivative matching for Maxwell's equations with material interfaces, J. Comput. Phys. 200 (2004) 60–103.
[41] S. Zhao, G.W. Wei, Matched interface and boundary (MIB) method for the implementation of boundary conditions in high-order central finite differences, Int. J. Numer. Methods Engrg. 77 (2009) 1690–1730.
[42] Y.C. Zhou, S. Zhao, M. Feig, G.W. Wei, High order matched interface and boundary (MIB) schemes for elliptic equations with discontinuous coefficients and singular sources, J. Comput. Phys. 213 (2006) 1–30.